Mon. Not. R. Astron. Soc. **369,** 156–170 (2006) doi:10.1111/j.1365-2966.2006.10278.x

X-ray spectra of sources in the 13$^{\rm H}$ *XMM–Newton*/*Chandra* deep field

M. J. Page,[1⋆] N. S. Loaring,[1] T. Dwelly,[1] K. O. Mason,[1] I. McHardy,[2] K. Gunn,[2] D. Moss,[2] T. Sasseen,[3] F. Cordova,[4] J. Kennea[5] and N. Seymour[6]

[1]*Mullard Space Science Laboratory, University College London, Holmbury St Mary, Dorking, Surrey RH5 6NT*
[2]*Department of Physics and Astronomy, University of Soutampton, Southampton SO17 1BJ*
[3]*Department of Physics, University of California, Santa Barbara, CA 93106, USA*
[4]*University of California, Riverside, 900 University Avenue, Riverside, CA 92521, USA*
[5]*Department of Astronomy and Astrophysics, 525 Davey Lab, Pennsylvania State University, University Park, PA 16802, USA*
[6]*Spitzer Science Center, California Institute of Technology, Mail Code 220-6, 1200 East California Boulevard, Pasadena, CA 91125, USA*

Accepted 2006 March 2. Received 2006 February 10; in original form 2005 October 9

ABSTRACT

We present the X-ray spectra of 86 optically identified sources in the 13$^{\rm H}$ *XMM–Newton*/*Chandra* deep field which have >70 X-ray counts. The majority of these sources have 2–10 keV fluxes between 10^{-15} and 5×10^{-14} erg cm^{-2} s^{-1}. The sample consists of 50 broad-line active galactic nuclei (BLAGN), 25 narrow emission-line galaxies (NELGs), six absorption-line galaxies and five Galactic stars. The majority (42/50) of the BLAGN have X-ray spectra which are consistent with a power-law shape. They have a mean photon index $\langle\Gamma\rangle = 2.0 \pm 0.1$ and an intrinsic dispersion $\sigma_\Gamma = 0.4 \pm 0.1$. Three of the BLAGN show curved spectra, with more emission near the high- and low-energy ends of the spectrum relative to the emission in the 1–2 keV range than can be reproduced by the power-law model. Five BLAGN show a deficit of soft X-rays, indicating absorption. We consider a source to be significantly absorbed if a power-law model fit is rejected with >99 per cent confidence and an absorbed power-law model produces an acceptable fit, or if the best-fitting power law is abnormally hard ($\Gamma < 1$). Significant absorption is more common in the NELGs (13/25) and absorption-line galaxies (2/6) than in the BLAGN (5/50), but is not universal in any of these classes of object. The majority of the 20 absorbed sources have X-ray spectra consistent with a simple cold photoelectric absorber, but a significant minority (6/20) require more complex models with either an additional component of soft X-ray emitting plasma, or an ionized absorber. Of the 16 narrow emission- and absorption-line galaxies which do not show evidence for X-ray absorption, only two objects are likely to be powered by star formation, and both have 2–10 keV X-ray luminosities of $\leqslant 10^{40}$ erg s^{-1}. The X-ray emission in the other 14 unabsorbed NELGs and galaxies is most likely powered by AGN, which are not detected in the optical because they are outshone by their luminous host galaxies. The Galactic stars show multitemperature thermal spectra which peak between 0.5 and 1 keV. Star/AGN discrimination is possible for four of the five stars solely from their X-ray spectra.

Key words: surveys – galaxies: active – quasars: general – X-rays: galaxies.

1 INTRODUCTION

The cosmic X-ray background (CXRB) is widely interpreted as the integrated X-ray emission from many discrete sources. Active galactic nuclei (AGN) are expected to contribute the majority of the CXRB, and since the late 1980s the leading 'synthesis models' have invoked a combination of absorbed and unabsorbed AGN to reproduce the overall intensity and broad-band spectral shape of the CXRB. Typically, these synthesis models are based on AGN 'unification schemes' (Antonucci 1993) in which each AGN contains an obscuring torus, and the orientation to our line of sight determines the absorption (e.g. Setti & Woltjer 1989; Comastri et al. 1995; Gilli, Risaliti & Salvati 1999).

⋆E-mail: mjp@mssl.ucl.ac.uk

The energy density of the CXRB peaks at ∼30 keV, but the CXRB has only been substantially resolved into sources at lower energies. In the 0.5–2 keV band, the deepest surveys with *ROSAT* resolved 70–80 per cent of the X-ray background into individual objects, the majority of which are broad-line AGN (BLAGN) (e.g. Hasinger et al. 1998; McHardy et al. 1998). Deep surveys performed with *XMM–Newton* and *Chandra* have increased the resolved fraction to 80–90 per cent in the 0.5–2 keV band, and have also resolved a significant fraction (>70 per cent) in the 2–10 keV band (e.g. Hasinger et al. 2001; Giacconi et al. 2002; Alexander et al. 2003). The broad-band X-ray spectral properties of the objects detected in the *XMM–Newton* and *Chandra* surveys support the hypothesis that the majority of the CXRB is due to AGN with a wide range of photoelectric absorption.

However, there have been a number of findings that are contrary to the assumptions and predictions of the synthesis models. Firstly, the optical and X-ray spectroscopic characteristics of the X-ray sources are sometimes discrepant. There are now many examples of AGN which appear to show photoelectric absorption from large column densities ($\geqslant 10^{22}$ cm^{-2}) of material, but which exhibit little attenuation to their optical and ultraviolet radiation (e.g. Maiolino et al. 2001; Page, Mittaz & Carrera 2001). On the other hand, there are also examples of AGN for which the broad optical emission lines are weak or absent, suggesting obscuration of the broad-line region by dust, but which show little or no absorption in their X-ray spectra (e.g. Pappa et al. 2001; Barcons, Carrera & Ceballos 2003; Mateos et al. 2005b).

Secondly the absorbed sources, and those without broad optical emission lines in their optical spectra (often referred to as 'type 2' AGN), are typically found at lower redshifts than predicted by the synthesis models (Barger et al. 2003, 2005; Mainieri et al. 2005). This suggests that the absorption properties of AGN have some dependence on either luminosity or redshift, in contrast to the very simple geometric unification schemes employed in the earlier versions of the synthesis models, which were independent of luminosity or redshift. However, this issue is still controversial (e.g. see Treister et al. 2004; Dwelly et al. 2005) and determining the absorption characteristics of AGN as a function of redshift and luminosity is one of the most important objectives of X-ray survey science.

The 13^H *XMM–Newton*/*Chandra* deep field is a project to investigate the astrophysics of the major contributors to the CXRB, particularly sources around the break in the X-ray source counts where the contribution to the CXRB per log-flux interval peaks. In order to understand the phenomena, processes and conditions in these sources we combine the high-quality X-ray spectra of *XMM–Newton* with the precise positions of *Chandra* and a host of other multiwavelength data, including a deep 1.4-GHz survey from the Very Large Array (Seymour, McHardy & Gunn 2004). The 13^H field is centred at $13^h34^m\ 37^s + 37^\circ54'44''$, was the location of one of the deepest *ROSAT* surveys (McHardy et al. 1998) and is a region of extremely low Galactic absorption ($N_H \sim 7 \times 10^{19}$ cm^{-2}).

In this paper, we present the European Photon Imaging Camera (EPIC, Strüder et al. 2001; Turner et al. 2001) spectra of the 13^H sources that have been optically identified and which have sufficient X-ray counts to yield a meaningful X-ray spectrum. At present, this amounts to 86 sources. Throughout this paper we assume $H_0 = 70$ km s^{-1} Mpc^{-1}, $\Omega_\Lambda = 0.7$, and $\Omega_m = 0.3$. We define a power-law spectrum as $dN/dE = AE^{-\Gamma}$ where N is the number of photons, E is photon energy, Γ is the photon index and A is the normalization. The source numbering scheme used here is identical to that used in Loaring et al. (2005).

2 X-RAY OBSERVATIONS AND DATA REDUCTION

The 13^H field was observed three times with *XMM–Newton* for a total exposure time of 200 ks. When dead time and periods of high background are excluded, the total live exposure time is 120 ks for the pn camera and 130 ks for each of the MOS cameras. The *XMM–Newton* observations are fully described in Loaring et al. (2005).

The EPIC spectra were produced from the same event lists, filtered with the same good time intervals, and using the same version of the *XMM–Newton* SCIENCE ANALYSIS SYSTEM (SAS 6.0) as the source lists presented in Loaring et al. (2005). Spectra were produced for all optically identified sources with >70 source counts. Source counts were accumulated in elliptical regions centred on the positions reported by Loaring et al. (2005). The size and ellipticity of each source extraction region was determined by the off-axis angle of the X-ray source, and its count rate. The point spread function (PSF) is relatively symmetrical near the centre of the *XMM–Newton* field of view but becomes elongated in the tangential direction at larger off-axis angles. Therefore, to optimize signal to noise the ellipticity of the source extraction regions increases with off-axis angle, from 0 at the optical axis to 2 near the edge of the field. The minor axes of our source regions vary from 10 to 20 arcsec depending on the overall source count rates. There are several pairs of sources which are close enough together that the nominal extraction regions would overlap. In such cases the two regions were renormalized so that they do not overlap, with the ratio of the minor axes set to the ratio of the count rates of the two sources.

All valid event patterns (PATTERN 0–12) were used in constructing the MOS spectra. For the pn spectra, single and double events (PATTERN 0–4) were used for channel energies >0.4 keV, and only single events were used for lower-energy channels. Channels close to the energies of the strongest instrumental emission lines (Cu K at 7.8 keV in pn and Al K at 1.7 keV in MOS) were excluded from the spectra. Response matrices and effective area files were constructed for each source region using the SAS tasks RMFGEN and ARFGEN, respectively. For each source the different EPIC spectra were combined to form a single spectrum over the 0.2–12 keV range, using the method of Page, Davis & Salvi (2003). Spectra were grouped to a minimum of 30 counts per bin.

3 OPTICAL SPECTROSCOPIC IDENTIFICATION

Optical spectroscopic observations were carried out in 2002 and 2003 at the William Herschel Telescope, using the AF2/WYFFOS multifibre positioner and spectrograph, and at the W. M. Keck observatory, using the LRIS and DEIMOS multi-object spectrographs. At present, 115 *XMM–Newton* and *Chandra* sources have optical spectroscopic identifications and redshifts. Full details of the observations and the optical spectra will be presented in Loaring et al. (in preparation).

4 RESULTS

There are 183 sources with >70 source counts in the 13^H field, 86 of which are optically identified. The majority of these identified sources have 2–10 keV fluxes in the range 10^{-15}–5×10^{-14} erg cm^{-2} s^{-1}. We have divided these 86 sources into four categories according to their optical spectroscopic properties: 50 BLAGN which have one or more emission lines with full width half-maximum (FWHM) >1000 km s^{-1}, 25 narrow emission-line galaxies (NELGs) which have emission lines of FWHM < 1000 km s^{-1},

Table 1. Power-law fits to the *XMM–Newton* spectra. A is the power-law normalization at 1 keV in units of 10^{-6} photons cm^{-2} s^{-1} keV^{-1}. z is the redshift of the source. P is the null hypothesis probability corresponding to χ^2/ν.

Source	z	Γ	A	χ^2/ν	P
BLAGN					
5	3.43	$1.89^{+0.63}_{-0.48}$	$2.4^{+0.7}_{-0.7}$	1/2	0.67
7	1.68	$2.60^{+0.47}_{-0.39}$	$1.0^{+0.3}_{-0.3}$	10/9	0.36
8	0.92	$1.75^{+0.66}_{-0.47}$	$2.5^{+0.8}_{-0.8}$	1/2	0.66
12	2.11	$1.73^{+0.38}_{-0.36}$	$1.1^{+0.2}_{-0.2}$	8/9	0.52
13	1.08	$2.22^{+0.15}_{-0.13}$	$13.6^{+1.1}_{-1.1}$	33/23	7.3×10^{-2}
19	0.97	$2.46^{+0.19}_{-0.17}$	$3.1^{+0.3}_{-0.3}$	18/17	0.38
24	0.73	$2.45^{+0.27}_{-0.25}$	$1.8^{+0.3}_{-0.3}$	10/15	0.82
27	2.81	$1.81^{+0.32}_{-0.29}$	$1.0^{+0.2}_{-0.2}$	12/9	0.20
30	2.14	$1.71^{+0.10}_{-0.10}$	$4.8^{+0.3}_{-0.3}$	57/36	1.5×10^{-2}
32	1.61	$1.92^{+0.08}_{-0.08}$	$8.8^{+0.4}_{-0.5}$	45/55	0.83
39	1.64	$1.68^{+0.11}_{-0.11}$	$4.1^{+0.3}_{-0.3}$	39/35	0.28
40	1.37	$0.21^{+0.51}_{-0.59}$	$0.14^{+0.10}_{-0.09}$	15/4	5.6×10^{-3}
41	1.60	$1.24^{+0.24}_{-0.24}$	$1.0^{+0.2}_{-0.2}$	12/9	0.22
42	1.34	$1.95^{+0.16}_{-0.16}$	$2.1^{+0.2}_{-0.2}$	32/18	2.0×10^{-2}
46	2.42	$1.84^{+0.18}_{-0.18}$	$1.7^{+0.2}_{-1.5}$	19/17	0.31
48	1.69	$1.78^{+0.19}_{-0.17}$	$1.4^{+0.2}_{-0.2}$	8/12	0.82
50	0.85	$1.63^{+0.07}_{-0.08}$	$5.2^{+0.3}_{-0.3}$	62/45	4.7×10^{-2}
52	0.39	$3.36^{+0.18}_{-0.17}$	$2.6^{+0.3}_{-0.3}$	60/30	1.0×10^{-3}
53	0.77	$2.62^{+0.25}_{-0.22}$	$2.0^{+0.3}_{-0.3}$	30/17	2.9×10^{-2}
60	2.47	$1.94^{+0.32}_{-0.29}$	$0.90^{+0.16}_{-0.17}$	8/9	0.56
65	1.14	$2.29^{+0.06}_{-0.06}$	$15.9^{+0.5}_{-0.5}$	153/98	3.2×10^{-4}
69	1.19	$1.93^{+0.23}_{-0.21}$	$1.4^{+0.2}_{-0.2}$	10/14	0.73
73	0.55	$1.71^{+0.35}_{-0.32}$	$1.4^{+0.3}_{-0.3}$	2/5	0.81
77	2.59	$2.05^{+0.25}_{-0.24}$	$2.0^{+0.3}_{-0.3}$	16/13	0.26
80	1.00	$1.47^{+0.48}_{-0.44}$	$0.71^{+0.22}_{-0.22}$	8/5	0.13
81	1.57	$2.12^{+0.18}_{-0.16}$	$2.9^{+0.3}_{-0.3}$	23/21	0.36
93	1.87	$2.14^{+0.42}_{-0.39}$	$0.55^{+0.12}_{-0.12}$	8/8	0.44
96	1.50	$0.99^{+0.16}_{-0.18}$	$0.85^{+0.16}_{-0.16}$	31/11	1.3×10^{-3}
97	1.36	$1.78^{+0.06}_{-0.06}$	$10.0^{+0.5}_{-0.5}$	72/62	0.19
101	0.52	$1.61^{+0.21}_{-0.19}$	$1.8^{+0.2}_{-0.2}$	47/20	6.3×10^{-4}
108	2.07	$1.59^{+0.40}_{-0.38}$	$0.42^{+0.12}_{-0.12}$	2/3	0.52
113	0.57	$2.08^{+0.08}_{-0.07}$	$7.4^{+0.3}_{-0.3}$	87/56	5.3×10^{-3}
119	0.26	$1.76^{+0.08}_{-0.08}$	$6.3^{+0.4}_{-0.4}$	40/50	0.79
121	1.14	$2.80^{+0.10}_{-0.10}$	$7.1^{+0.4}_{-0.4}$	57/56	0.46
129	1.89	$2.25^{+0.19}_{-0.18}$	$1.8^{+0.2}_{-0.2}$	15/18	0.65
132	0.71	$1.10^{+0.08}_{-0.09}$	$4.4^{+0.4}_{-0.4}$	115/31	1.4×10^{-11}
134	1.18	$1.22^{+0.07}_{-0.08}$	$4.0^{+0.3}_{-0.3}$	73/39	7.5×10^{-4}
143	1.89	$1.95^{+0.10}_{-0.09}$	$5.9^{+0.3}_{-0.3}$	46/45	0.45
161	2.01	$2.18^{+0.42}_{-0.37}$	$0.99^{+0.23}_{-0.23}$	3/7	0.88
162	1.77	$1.99^{+0.28}_{-0.25}$	$1.0^{+0.2}_{-0.2}$	13/10	0.25
164	1.49	$2.34^{+0.77}_{-0.68}$	$0.39^{+0.13}_{-0.15}$	8/5	0.18
173	2.48	$2.13^{+0.27}_{-0.26}$	$1.3^{+0.2}_{-0.2}$	14/11	0.25
178	2.66	$1.75^{+0.50}_{-0.45}$	$0.45^{+0.12}_{-0.14}$	3/4	0.62
190	2.82	$1.93^{+0.20}_{-0.20}$	$2.3^{+0.3}_{-0.3}$	15/15	0.42
196	1.38	$1.53^{+0.21}_{-0.21}$	$2.0^{+0.3}_{-0.3}$	11/10	0.33
208	1.39	$2.01^{+0.16}_{-0.16}$	$4.7^{+0.4}_{-0.4}$	17/23	0.79
212	1.63	$2.04^{+0.11}_{-0.10}$	$8.7^{+0.6}_{-0.6}$	32/35	0.63
217	2.28	$1.61^{+0.20}_{-0.20}$	$2.6^{+0.4}_{-0.4}$	16/13	0.23
218	1.89	$1.84^{+0.20}_{-0.19}$	$3.6^{+0.4}_{-0.4}$	30/17	2.7×10^{-2}
221	1.62	$1.85^{+0.12}_{-0.12}$	$9.1^{+0.7}_{-0.7}$	34/33	0.40
NELGs					
1	0.39	$2.09^{+0.57}_{-0.49}$	$2.5^{+0.7}_{-0.7}$	1/1	0.48
20	0.17	$2.53^{+0.31}_{-0.27}$	$1.3^{+0.2}_{-0.2}$	4/7	0.77
56	0.06	$2.54^{+0.58}_{-0.49}$	$0.46^{+0.17}_{-0.18}$	12/4	1.7×10^{-2}
62	0.43	$0.60^{+0.99}_{-1.00}$	$0.18^{+0.15}_{-0.13}$	5/3	0.18
66	0.29	$0.64^{+0.61}_{-0.44}$	$0.26^{+0.15}_{-0.14}$	1/3	0.77
67	0.34	$0.70^{+0.09}_{-0.10}$	$1.8^{+0.2}_{-0.2}$	111/30	3.0×10^{-11}
76	0.49	$-0.12^{+0.57}_{-0.75}$	$0.11^{+0.10}_{-0.08}$	3/4	0.60
94	0.85	$1.45^{+0.53}_{-0.52}$	$0.21^{+0.09}_{-0.09}$	6/3	9.8×10^{-2}
100	0.27	$0.52^{+0.72}_{-0.75}$	$0.28^{+0.17}_{-0.15}$	14/3	3.6×10^{-3}
103	0.55	$1.51^{+0.15}_{-0.14}$	$1.4^{+0.2}_{-0.2}$	29/18	4.3×10^{-2}
109	0.57	$0.59^{+0.09}_{-0.10}$	$1.5^{+0.2}_{-0.2}$	87/24	4.7×10^{-9}
115	0.23	$1.85^{+0.14}_{-0.13}$	$4.6^{+0.4}_{-0.4}$	17/25	0.88
118	0.06	$1.95^{+0.49}_{-0.44}$	$0.37^{+0.11}_{-0.11}$	3/5	0.76
126	1.09	$0.42^{+0.68}_{-0.70}$	$0.13^{+0.11}_{-0.07}$	7/3	7.2×10^{-2}
131	0.22	$2.03^{+0.51}_{-0.45}$	$0.37^{+0.11}_{-0.12}$	4/4	0.36
142	0.31	$0.69^{+0.11}_{-0.11}$	$1.4^{+0.2}_{-0.2}$	101/23	9.2×10^{-12}
153	0.43	$1.87^{+0.57}_{-0.52}$	$0.33^{+0.12}_{-0.12}$	4/3	0.22
165	0.56	$0.92^{+0.16}_{-0.17}$	$1.00^{+0.2}_{-0.2}$	26/13	1.6×10^{-2}
175	0.36	$1.66^{+0.12}_{-0.12}$	$4.6^{+0.4}_{-0.4}$	68/34	5.0×10^{-4}
186	0.81	$1.60^{+0.32}_{-0.30}$	$0.96^{+0.18}_{-0.18}$	1/5	0.94
193	0.12	$2.11^{+0.62}_{-0.49}$	$0.63^{+0.20}_{-0.20}$	2/4	0.69
200	0.88	$1.36^{+0.35}_{-0.34}$	$0.80^{+0.20}_{-0.20}$	5/7	0.62
213	0.80	$0.15^{+0.22}_{-0.24}$	$1.0^{+0.3}_{-0.3}$	16/7	2.4×10^{-2}
222	0.26	$0.91^{+0.22}_{-0.22}$	$2.3^{+0.5}_{-0.5}$	17/10	7.4×10^{-2}
225	0.26	$2.08^{+0.41}_{-0.36}$	$1.8^{+0.5}_{-0.5}$	17/4	2.0×10^{-3}
Galaxies					
37	0.26	$2.19^{+0.13}_{-0.12}$	$3.7^{+0.3}_{-0.3}$	16/18	0.62
55	1.08	$2.10^{+0.28}_{-0.25}$	$1.0^{+0.2}_{-0.2}$	4/10	0.94
92	0.29	$0.56^{+0.18}_{-0.18}$	$0.51^{+0.12}_{-0.12}$	37/12	2.6×10^{-4}
98	0.36	$-0.24^{+0.49}_{-0.58}$	$0.08^{+0.07}_{-0.05}$	12/5	3.5×10^{-2}
117	0.62	$2.02^{+0.67}_{-0.64}$	$0.57^{+0.21}_{-0.21}$	9/4	6.0×10^{-2}
184	0.55	$1.55^{+0.31}_{-0.28}$	$1.8^{+0.3}_{-0.3}$	14/10	0.16
Stars					
49	–	$2.09^{+0.16}_{-0.16}$	$2.6^{+0.3}_{-0.3}$	37/19	7.1×10^{-3}
61	–	$3.09^{+0.18}_{-0.16}$	$1.3^{+0.2}_{-0.2}$	110/19	6.8×10^{-15}
120	–	$2.45^{+0.26}_{-0.25}$	$1.9^{+0.3}_{-0.4}$	31/11	1.1×10^{-3}
140	–	$2.56^{+0.01}_{-0.01}$	163^{+2}_{-2}	8027/165	$<10^{-30}$
179	–	$1.96^{+0.81}_{-0.64}$	$0.53^{+0.20}_{-0.20}$	2/4	0.70

six absorption-line galaxies which do not exhibit any emission lines in our optical spectra (hereafter simply 'galaxies'), and five Galactic stars.

As a starting point for the X-ray spectral investigations we fitted each spectrum with a power-law model, and fixed Galactic absorption ($N_{\rm H} = 7 \times 10^{-19}$ cm^{-2}). The results of these fits are given in Table 1. The individual spectra, grouped by optical counterpart

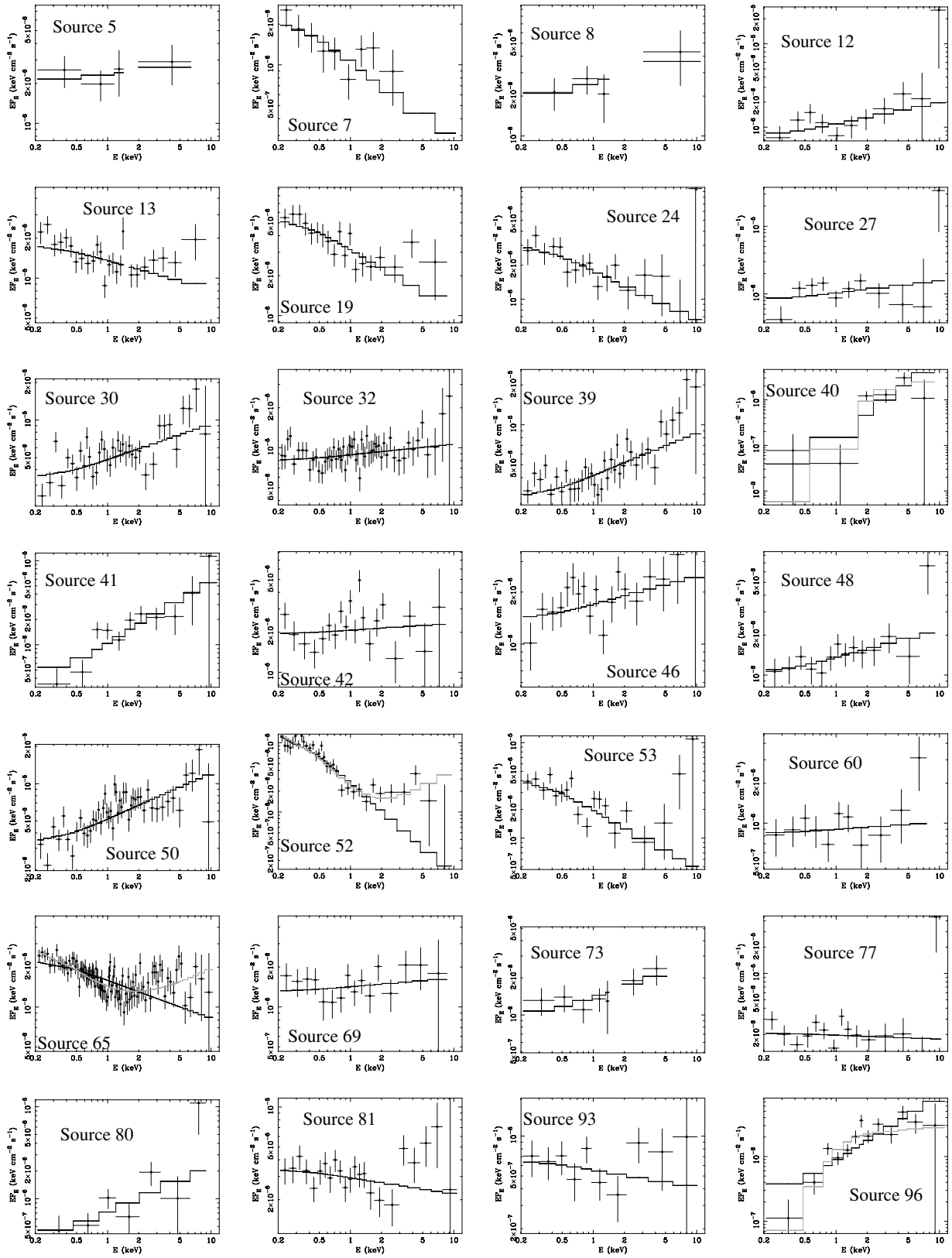

Figure 1. X-ray spectra of the BLAGN (data points) together with power-law models (black stepped lines). All spectra are shown in the observer frame. Both model and data have been divided by the product of the effective area and Galactic transmission as a function of energy. For those objects which required a more complex spectral model, this is shown as a grey stepped line. For sources 52, 65 and 113 the grey line is the two power-law model. For sources 40, 96 and 134, the grey line is a power law with cold absorption intrinsic to the AGN. For source 101 the grey line is a power law with an ionized absorber, and for source 132 the grey line is an absorbed power law with an optically thin thermal plasma contributing at soft energies.

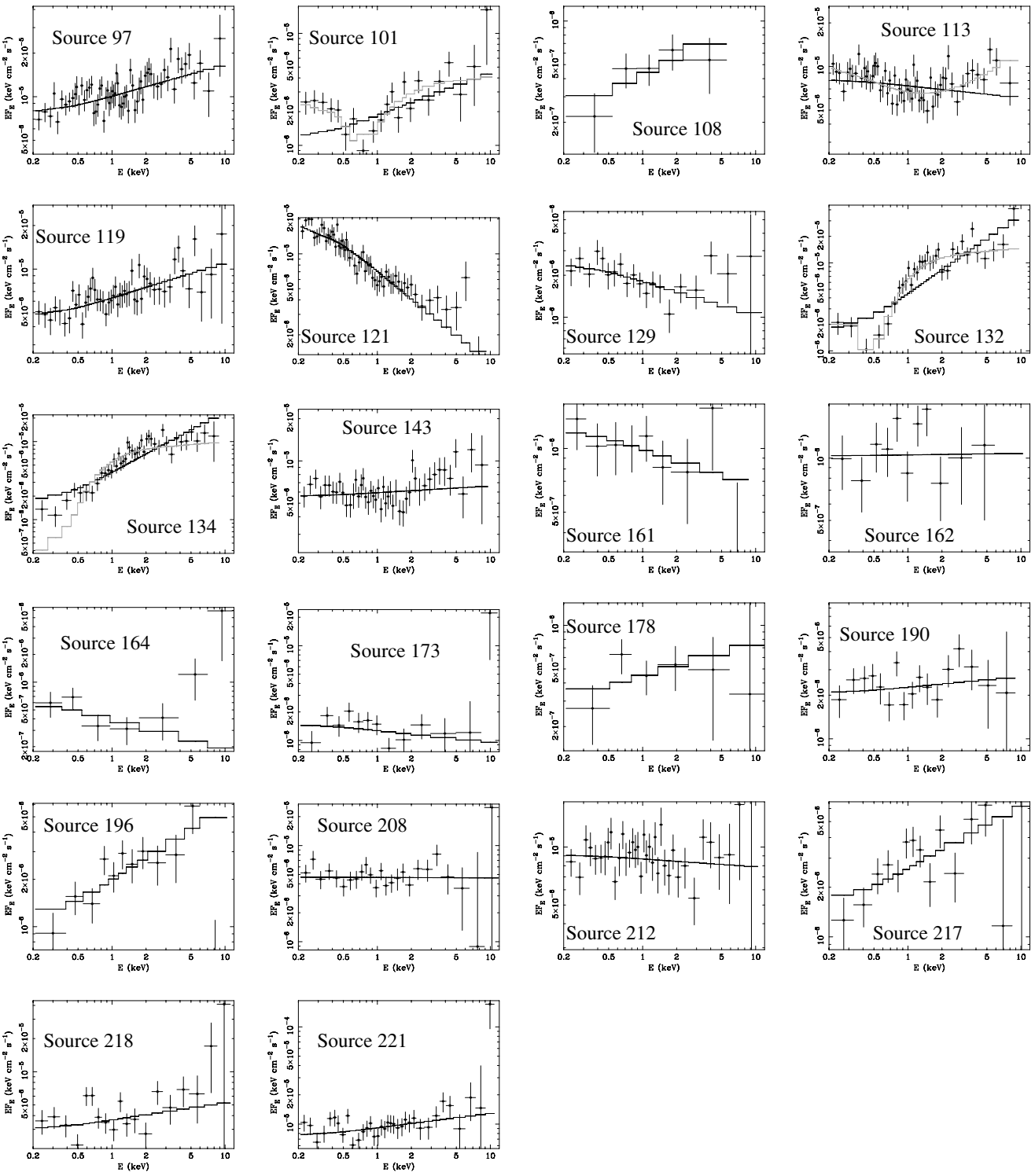

Figure 1 – *continued*

type, are shown along with the best-fitting power-law models in Figs 1–4. In order to show the intrinsic shapes of the spectra, both the spectra and the models in Figs 1–4 have been divided by the product of the EPIC effective area and the Galactic transmission on a channel-by-channel basis. For the sample size of 86 spectra, we consider a null hypothesis probability of 1 per cent to be an appropriate threshold between acceptable and unacceptable goodness of fit. We now describe the EPIC spectral fits for each of the four optical spectroscopic subclasses.

4.1 BLAGN

The BLAGN represent the largest subsample, numbering 50 sources. The power-law model is quite successful for these sources:

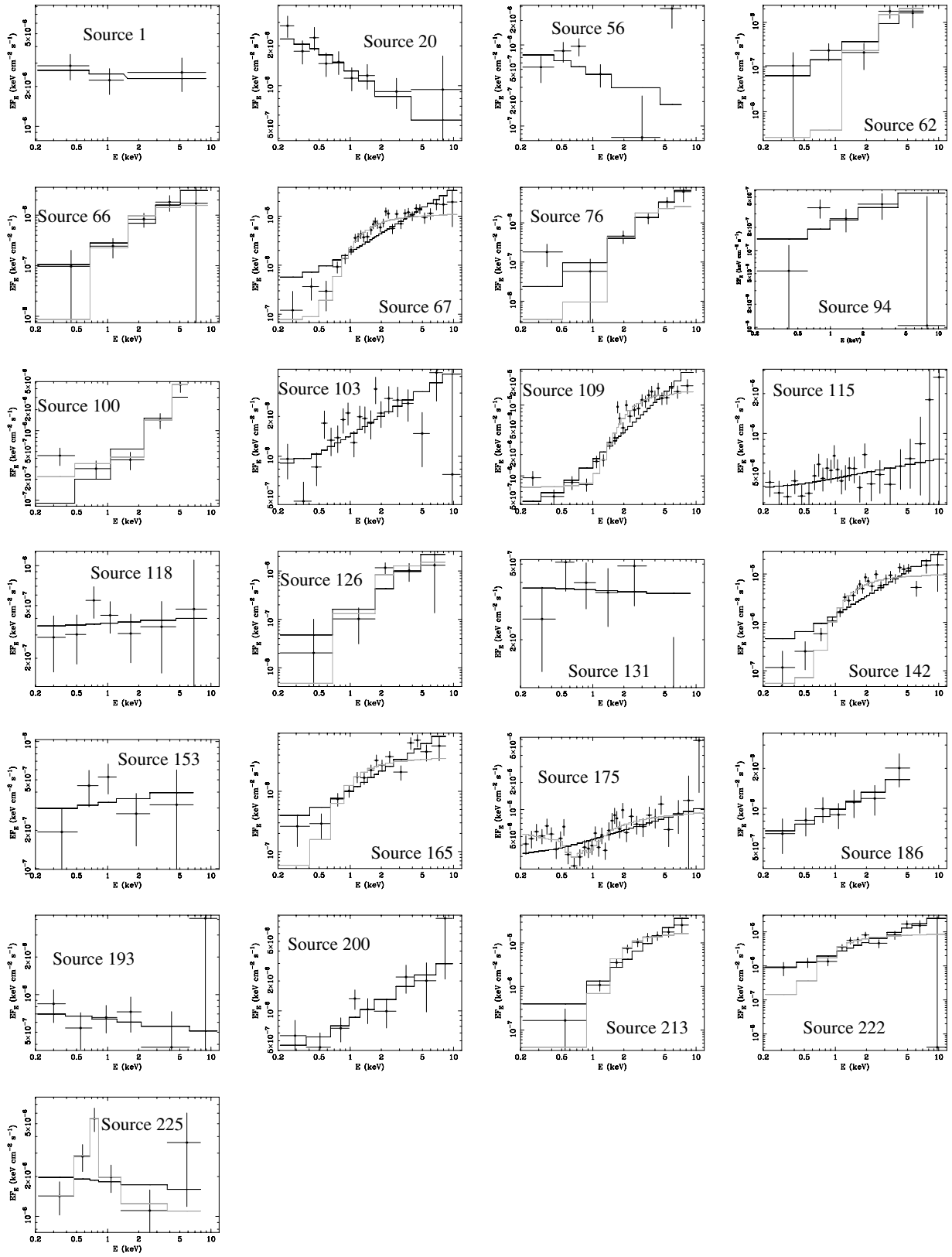

Figure 2. X-ray spectra of the NELGs (data points) together with power-law models (black stepped lines). All spectra are shown in the observer frame. Both model and data have been divided by the product of effective area and Galactic transmission as a function of energy. For those sources which were fitted with more complex models, the best fit is shown as a grey stepped line. For sources 62, 66, 67, 76, 126, 142, 165, 213 and 222 the grey line is a power-law model with cold absorption. For source 175 the grey line shows a power law with an ionized absorber, and for source 109 the grey line is an absorbed power law with a second, unabsorbed, power-law component. For sources 100 and 225, the grey line shows an absorbed power law with an optically thin thermal plasma contributing at soft energies.

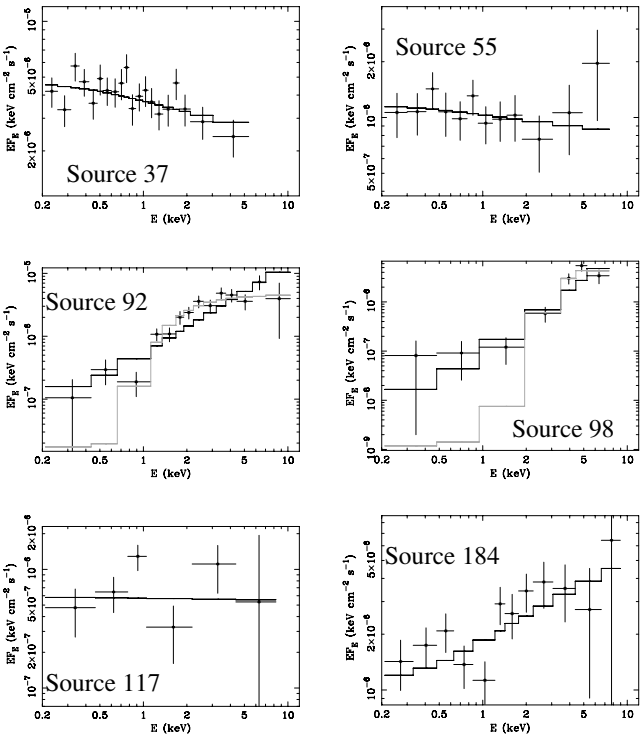

Figure 3. X-ray spectra of the galaxies (data points) together with power-law models (black stepped lines). All spectra are shown in the observer frame. Both model and data have been divided by the product of effective area and Galactic transmission as a function of energy. For sources 92 and 98 a better fitting model of a power law absorbed by cold material is also shown, as a grey stepped line.

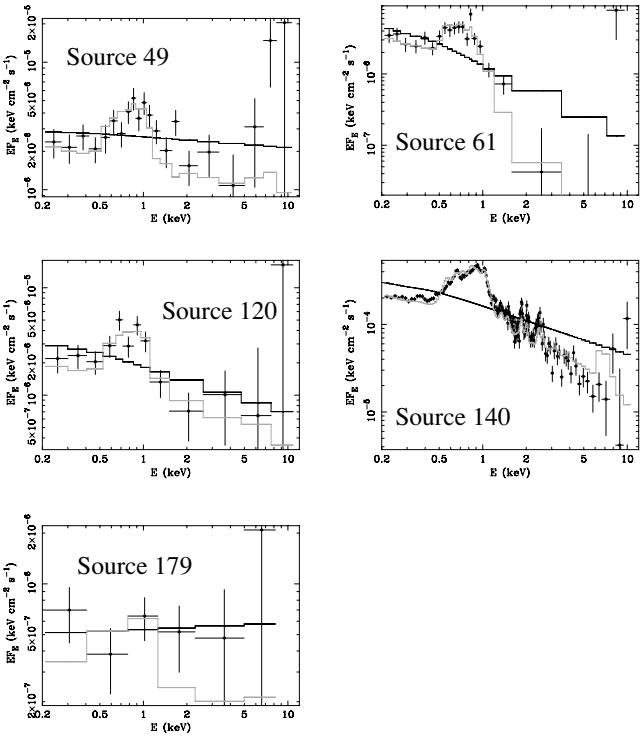

Figure 4. X-ray spectra of the Galactic stars (data points) together with power-law models (black stepped lines) and multitemperature optically thin thermal models (grey stepped lines). All spectra are shown in the observer frame. Both models and data have been divided by the product of effective area and Galactic transmission as a function of energy.

Table 2. Power-law fits including cold photoelectric absorption and with fixed $\Gamma = 1.9$. A is the power-law normalization in units of 10^{-6} photons cm^{-2} s^{-1} keV^{-1}. Sources marked with an '*' have acceptable χ^2 with a simple power-law fit, but have been fitted with the model including cold absorption because they have best-fitting $\Gamma < 1$. Parameters and uncertainties marked with † are constrained by the maximum or minimum of the allowed range. P is the null hypothesis probability corresponding to χ^2/ν.

Source	A	$N_{\rm H}$ (10^{22} cm^{-2})	χ^2/ν	P
BLAGN				
40	$2.2^{+1.4}_{-1.0}$	19^{+20}_{-9}	5/4	0.34
96	$2.3^{+0.6}_{-0.5}$	$2.5^{+1.7}_{-1.0}$	18/11	7.6×10^{-2}
101	$1.8^{+0.2}_{-0.2}$	$0.00\dagger^{+0.04}_{-0.00\dagger}$	54/20	5.6×10^{-5}
132	$11.3^{+1.2}_{-1.1}$	$0.83^{+0.19}_{-0.16}$	53/31	8.2×10^{-3}
134	$7.9^{+0.8}_{-0.8}$	$1.00^{+0.30}_{-0.24}$	58/39	2.4×10^{-2}
NELGs				
62*	$2.1^{+2.1}_{-1.9}$	$9.5^{+19.6}_{-9.4}$	7/3	7.2×10^{-2}
66*	$1.3^{+1.2}_{-0.7}$	$1.7^{+3.9}_{-1.2}$	1/3	0.70
67	$8.7^{+1.1}_{-1.0}$	$1.17^{+0.25}_{-0.20}$	38/30	0.15
76*	$2.4^{+9.7}_{-1.2}$	$9.7^{+61.8}_{-6.3}$	8/4	0.11
109	$11.5^{+1.6}_{-1.5}$	$4.0^{+0.9}_{-0.7}$	97/24	8.6×10^{-11}
126*	$1.4^{+1.0}_{-0.7}$	10^{+14}_{-6}	2/3	0.63
142	$7.7^{+1.1}_{-1.0}$	$1.4^{+0.3}_{-0.3}$	31/23	0.13
165*	$2.9^{+0.6}_{-0.6}$	$0.96^{+0.48}_{-0.33}$	22/13	5.1×10^{-2}
175	$4.7^{+0.6}_{-0.4}$	$0.01^{+0.03}_{-0.01\dagger}$	82/34	8.5×10^{-6}
184	$0.4^{+0.3}_{-0.1}$	$0.01^{+0.26}_{-0.01\dagger}$	25/3	1.4×10^{-5}
213*	$14.3^{+4.4}_{-3.7}$	$8.6^{+4.1}_{-2.6}$	5/7	0.62
222*	$6.9^{+1.9}_{-1.8}$	$0.64^{+0.34}_{-0.27}$	21/10	2.0×10^{-2}
225	$1.9^{+0.6}_{-0.5}$	$0.00\dagger^{+0.06}_{0.00\dagger}$	18/4	1.3×10^{-3}
Galaxies				
92	$3.7^{+0.9}_{-0.8}$	$2.1^{+0.8}_{-0.6}$	15/12	0.26
98*	$5.9^{+4.7}_{-2.6}$	25^{+22}_{-12}	7/5	0.20

42 can be fitted acceptably with the power-law model, and eight cannot be. The mean best-fitting spectral index of the acceptably fitted sources is $\langle\Gamma\rangle = 1.90 \pm 0.06$.

Inspection of Fig. 1 reveals that the poorly fitting spectra deviate from a power-law shape in several different ways. Just over half of the poor-fitting spectra are relatively hard (sources 40, 96, 101, 132 and 134), while the other three are relatively soft (sources 52, 65 and 113). The hard spectrum sources could deviate from power-law shapes because they are photoelectrically absorbed. Therefore, we refitted these spectra, including photoelectric absorption from cold gas at the same redshift as the AGNs. To minimize the number of free parameters in the fit, we fixed the power-law slopes at a 'typical' BLAGN value of $\Gamma = 1.9$ and assumed Galactic abundances (Anders & Grevesse 1989). The results are given in Table 2. For three of the sources acceptable fits were obtained, while for source 132 the fit was significantly better than the simple power-law fit, though still rejected at 99 per cent confidence. However, for source 101 there was no improvement to the χ^2 compared to the power-law model, and the best-fitting column density is zero. For source 132, the largest contribution to χ^2 comes from the two lowest-energy channels, which are in excess of the model, while for source 101 there is a minimum around 0.7 keV (observed frame) which the model cannot reproduce.

There are several reasonable modifications to the absorption model that might better reproduce the spectra of sources 101 and 132. Firstly, there might be some extra emission component at the softest energies. We tried two variants of such a model: one including an emission-line component, modelled as a low-temperature thermal plasma (mekal in XSPEC), and one including a component of unabsorbed power-law emission. Soft X-ray emission lines are prominent in the spectra of nearby Seyfert 2 galaxies (e.g. Sako et al. 2001; Kinkhabwala et al. 2002), and although they are photoionized rather than collisionally ionized, the mekal model is a reasonable approximation at the resolution and signal to noise ratio of our EPIC spectra. On the other hand, an unabsorbed power-law component could represent primary emission that has been scattered into our line of sight, bypassing the absorbing medium. Such a model has been used widely (e.g. Turner et al. 1997; Franceschini et al. 2003; Caccianiga et al. 2004) and has a simple and convenient functional form. The results for these two fits are given in Tables 3 and 4. The model with an unabsorbed power-law component fits the spectrum of source 132, but not the spectrum of source 101. The model including a soft thermal component provides a good fit to the spectra of both objects.

Table 3. Absorbed power-law fits with an additional unabsorbed power-law component. A_1 is the normalization of the primary, absorbed power law and A_2 is the normalization of the secondary, unabsorbed power law, both in units of 10^{-6} photons cm^{-2} s^{-1} keV^{-1}. Parameters and uncertainties marked with † are constrained by the limits of the fit range. P is the null hypothesis probability corresponding to χ^2/ν.

Source	A_1	A_2	$N_{\rm H}$ (10^{22} cm^{-2})	χ^2/ν	P
BLAGN					
101	$1.7^{+1.4}_{-0.9}$	$1.6^{+0.3}_{-0.3}$	$3.5^{+15.2}_{-2.0}$	38/19	6.8×10^{-3}
132	$10.8^{+1.3}_{-1.3}$	$1.2^{+0.6}_{-0.6}$	$1.2^{+0.4}_{-0.3}$	39/30	0.12
NELGs					
100	$6.6^{+14.3}_{-4.3}$	$0.35^{+0.12}_{-0.12}$	29^{+49}_{-20}	1/2	0.51
109	$12.2^{+1.7}_{-1.6}$	$0.72^{+0.17}_{-0.17}$	$5.9^{+1.4}_{-1.1}$	28/23	0.20
175	$3.5^{+1.5}_{-1.4}$	$4.0^{+0.4}_{-0.5}$	$2.5^{+2.8}_{-1.3}$	54/33	1.2×10^{-2}
225	$1.9^{+0.5}_{-1.9\dagger}$	$0.00\dagger^{+2.3}_{-0.0\dagger}$	$0^{+1000\dagger}_{-0\dagger}$	18/3	4.5×10^{-4}

Table 4. Absorbed power-law fits with an additional soft emission-line component, modelled as a 'mekal' thermal plasma. A is the normalization of the power-law component in units of 10^{-6} photons cm^{-2} s^{-1} keV^{-1}. norm$_{\rm mek}$ is the normalization of the thermal plasma given as $\int n_{\rm e} n_{\rm H} {\rm d}V/(4\pi D_l^2)$ in units of 10^{-20} cm^{-5}, where $n_{\rm e}$ and $n_{\rm H}$ are the electron and hydrogen number densities, respectively, V is volume and D_l is the luminosity distance. Parameters and uncertainties marked with † are constrained by the limits of the fit range. P is the null hypothesis probability corresponding to χ^2/ν.

Source	A	$N_{\rm H}$ (10^{22} cm^{-2})	kT (keV)	norm$_{\rm mek}$	χ^2/ν	P
BLAGN						
101	$2.9^{+0.6}_{-0.6}$	$0.70^{+0.38}_{-0.30}$	$0.21^{+0.04}_{-0.03}$	$1.7^{+0.6}_{-0.4}$	19/18	0.39
132	$11.7^{+1.2}_{-1.2}$	$0.94^{+0.21}_{-0.18}$	$0.16^{+0.08}_{-0.06}$	$2.1^{+12.3}_{-1.4}$	33/29	0.30
NELG						
100	$6.5^{+23.0}_{-4.4}$	29^{+94}_{-19}	$4.3^{+5.8}_{-4.1}$	$1.1^{+0.5}_{-0.5}$	4/1	5.4×10^{-2}
109	$11.7^{+2.4}_{-1.6}$	$6.7^{+1.8}_{-1.3}$	$10.0^{+0.0\dagger}_{-5.2}$	$2.7^{+0.6}_{-1.2}$	28/22	0.18
175	$6.7^{+1.0}_{-0.9}$	$0.41^{+0.22}_{-0.16}$	$0.19^{+0.04}_{-0.03}$	$3.4^{+1.3}_{-0.8}$	41/32	0.14
225	$0.9^{+7.5}_{-0.8}$	$0.02^{+11.50}_{-0.02}$	$0.77^{+0.40}_{-0.17}$	$1.6^{+1.1}_{-0.8}$	1/2	0.55

Table 5. Power-law fits with fixed $\Gamma = 1.9$ and an ionized absorber. A is the power-law normalization in units of 10^{-6} photons cm^{-2} s^{-1} keV^{-1}. ξ is the ionization parameter in units of erg cm s^{-1}. Parameters and uncertainties marked with † are constrained by the limits of the fit range. P is the null hypothesis probability corresponding to χ^2/ν.

Source	A	ξ	$N_{\rm H}$ (10^{22} cm^{-2})	χ^2/ν	P
BLAGN					
101	$3.3^{+0.6}_{-0.6}$	140^{+180}_{-80}	$2.6^{+2.4}_{-1.4}$	21/19	0.35
132	$12.0^{+1.2}_{-1.2}$	$3.9^{+5.7}_{-3.0}$	$1.4^{+0.4}_{-0.3}$	34/30	0.28
NELGs					
100	$2.1^{+1.7}_{-1.2}$	60^{+120}_{-40}	7^{+9}_{-5}	12/2	3.0×10^{-3}
109	$11.8^{+1.6}_{-1.5}$	$3.8^{+5.7}_{-3.0}$	$6.8^{+1.6}_{-1.3}$	59/23	5.2×10^{-5}
175	$7.3^{+1.0}_{-0.9}$	60^{+80}_{-40}	$1.3^{+0.9}_{-0.6}$	34/33	0.40
225	$1.9^{+0.6}_{-0.5}$	$0\dagger^{+1000\dagger}_{-0\dagger}$	$0\dagger^{+50}_{-0\dagger}$	18/3	4.5×10^{-4}

Table 6. Power-law and cold reflection model fits to X-ray spectra of BLAGN. A is the power-law normalization in units of 10^{-6} photons cm^{-2} s^{-1} keV^{-1}. The reflection fraction R is the size of the reflection component relative to a plane reflector covering 2π sr. P is the null hypothesis probability corresponding to χ^2/ν.

Source	Γ	A	R	χ^2/ν	P
52	$3.60^{+0.25}_{-0.22}$	$2.0^{+0.5}_{-0.5}$	125^{+157}_{-75}	41/29	6.6×10^{-2}
65	$2.58^{+0.13}_{-0.11}$	$13.0^{+1.1}_{-1.2}$	$13.8^{+8.1}_{-5.3}$	93/97	0.59
113	$2.31^{+0.14}_{-0.14}$	$6.5^{+0.5}_{-0.6}$	$12.7^{+10.2}_{-6.5}$	63/55	0.21

The alternative to an additional soft component, is that the absorbing material is ionized, in which case the strongest absorption features will occur at higher energies than in a cold absorber, and there may be no need for additional soft X-ray components in sources 101 and 132. Therefore, we replaced the component of cold absorption with an ionized absorber ('absori' in XSPEC), and refitted the spectra of sources 101 and 132, again assuming $\Gamma = 1.9$ and Galactic abundances. The results are given in Table 5 and show that this model fits both spectra well.

Absorption, either by cold or ionized gas, is unlikely to explain the poor fit of the power-law model to sources 52, 65 and 113, which have relatively soft spectra (best-fitting $\Gamma > 2$). In all three cases, the data systematically exceed the model at energies $\geqslant$2 keV, indicating that the spectra are curved relative to a power law, or that there is more than one broad-band component in the spectrum. We have explored two models for these spectra: a power law with a reflection component, and a two power-law model, which will produce a curved continuum. The results of the reflection fits are given in Table 6. In all three cases, the χ^2 values indicate acceptable fits when the reflection component is included, but the degree of reflection required is far too large to be physically realistic. The results of the double power-law fits are given in Table 7. The goodness of fit is acceptable in all three cases.

4.2 NELGs

The power-law model was fitted to the NELG X-ray spectra and yielded acceptable fits in 19/25 cases (Table 1). Of the six NELGs for which the power-law model is rejected at >99 per cent confidence,

Table 7. Fits with two power laws to X-ray spectra of BLAGN. A_1 and A_2 are the normalizations in units of 10^{-6} photons cm^{-2} s^{-1} keV^{-1} for the power laws with photon indices Γ_1 and Γ_2, respectively. P is the null hypothesis probability corresponding to χ^2/ν.

Source	Γ_1	A_1	Γ_2	A_2	χ^2/ν	P
52	$3.65^{+0.36}_{-0.26}$	$2.0^{+0.5}_{-0.7}$	$1.03^{+0.81}_{-0.89}$	$0.47^{+0.73}_{-0.36}$	42/28	4.3×10^{-2}
65	$2.97^{+0.60}_{-0.35}$	$7.4^{+4.6}_{-4.5}$	$1.57^{+0.31}_{-0.48}$	$7.0^{+4.6}_{-4.3}$	96/96	0.48
113	$2.69^{+0.88}_{-0.40}$	$3.8^{+2.6}_{-2.9}$	$1.37^{+0.42}_{-0.79}$	$2.8^{+1.9}_{-2.3}$	61/54	0.24

four have best-fitting $\Gamma < 1$, suggesting that the poor fits are due to photoelectric absorption. A further seven NELGs with acceptable power-law spectral fits have best-fitting $\Gamma < 1$. Such a hard spectral shape is unlikely to be the intrinsic continuum of an AGN. Therefore, we refitted all of the sources which are not well fitted by the power-law model, and all of the sources with best-fitting $\Gamma < 1$, with a $\Gamma = 1.9$ power law absorbed by a neutral column of material at the same redshift as the object. The results are given in Table 2. Acceptable fits are found for all of the sources except for 100, 109, 175 and 225. We refitted these four spectra using the same set of models as for the BLAGN which could not be fitted with the cold absorption model. The fit with an additional unabsorbed power law yields an acceptable χ^2 for sources 100, 109 and 175, but not for source 225 (Table 3), while the fit with a soft emission-line component produces acceptable χ^2 for all four objects (Table 4). The ionized absorption model is less successful: it produces a reasonable fit for source 175 but not for the other three objects (Table 5). Source 225 can only be adequately fitted when a soft thermal component is included, and in this case there is no requirement that the power-law component is absorbed.

Of course it is possible that those NELGs which are well fitted by a $\Gamma > 1$ power law and no intrinsic absorption could still harbour absorption at a level that is too small to be detected in our X-ray spectra. Therefore, for these 12 NELGs we have determined upper limits to the intrinsic column densities by fitting with a power-law and intrinsic absorption, and increasing the column density until $\Delta\chi^2 = 4$, corresponding to the 95 per cent upper limit. To be conservative, we allowed Γ to vary freely up to a maximum of $\Gamma = 2.5$. The results are given in Table 8; the majority of the sources have upper limits to $N_{\rm H}$ which are $\leqslant 3 \times 10^{21}$ cm^{-2}.

4.3 Absorption-line galaxies

Of the six absorption-line galaxies, only source 92 is poorly fitted with the power-law model (see Table 1). This object, and source 98, require very hard spectral indices ($\Gamma < 1$), so we refitted these two spectra with a $\Gamma = 1.9$ power-law and cold photoelectric absorption. In both cases this provides an acceptable fit, as seen in Table 2.

For the four sources which were well fitted with a ($\Gamma > 1$) power-law model, we have worked out 95 per cent upper limits to the amount of absorption which could be present by adding intrinsic photoelectric absorption to the power-law model, and increasing the column density until $\Delta\chi^2 = 4$; the results are given in Table 8.

4.4 Galactic stars

We began with a power-law fit to the stars including full Galactic absorption, exactly as for the extragalactic sources. The results are listed in Table 1, and the spectra are shown in Fig. 4. The power-law model is rejected in four of the five stars, which show a distinctive emission peak between 0.5 and 1 keV, indicating optically thin thermal emission. However, the power-law model is an acceptable fit to the X-ray spectrum of source 179, which has by far the lowest quality spectrum. We next applied a single-temperature optically thin thermal model (mekal). This model also failed to produce acceptable fits for four out of five stars (see Table 9): the stellar X-rays are distributed over a larger energy range than the model spectra. Therefore, we fitted a multitemperature mekal model that has a uniform distribution of emission measure with temperature up to a maximum temperature T. The results of this model fit are listed in Table 10 and shown in Fig. 4. This model produced acceptable fits to the X-ray spectra of all the stars except source 140. However, inspection of Fig. 4 indicates that despite the large χ^2, the model reproduces the shape of the spectrum of source 140 quite well, but not in detail. Source 140 has the highest signal/noise X-ray spectrum by far within the 13$^{\rm H}$ field; a more complex model would be required to reproduce the details, but this is beyond the scope of this paper.

Table 8. 95 per cent upper limits to the intrinsic column densities of the NELGs and galaxies which are well fit with a $\Gamma > 1$ power-law model.

Source	$N_{\rm H}$ 95 per cent upper limit (10^{22}cm^{-2})
NELGs	
1	0.17
20	0.026
56	0.077
94	3.6
103	0.30
115	0.12
118	0.68
131	0.50
153	1.68
186	0.23
193	0.26
200	0.62
Galaxies	
37	0.096
55	0.22
117	3.1
184	0.070

Table 9. Single-temperature optically thin thermal plasma (mekal) fits to the *XMM–Newton* spectra of the Galactic stars. norm$_{\rm mek}$ is the normalization of the thermal plasma given as $\int n_{\rm e} n_{\rm H} {\rm d}V/(4\pi D^2)$ in units of 10^{-20} cm^{-5}, where $n_{\rm e}$ and $n_{\rm H}$ are the electron and hydrogen number densities, respectively, V is volume and D is the distance. Parameters and uncertainties marked with † are constrained by the limits of the fit range. P is the null hypothesis probability corresponding to χ^2/ν.

Source	kT	norm$_{\rm mek}$ (keV)	χ^2/ν	P
49	$2.44^{+0.77}_{-0.49}$	$7.6^{+1.0}_{-1.1}$	51/19	8.6×10^{-5}
61	$0.26^{+0.01}_{-0.02}$	$3.0^{+0.3}_{-0.3}$	43/18	8.3×10^{-4}
120	$0.29^{+0.05}_{-0.03}$	$2.3^{+0.4}_{-0.4}$	37/11	1.1×10^{-4}
140	$0.68^{+0.01}_{-0.01}$	192^{+3}_{-2}	9645/165	$<10^{-30}$
179	$2.9^{+17.1\dagger}_{-1.6}$	$1.6^{+1.3}_{-0.8}$	3/4	0.56

Table 10. Multitemperature optically thin thermal plasma (cemekl) fits to the *XMM–Newton* spectra of the Galactic stars, with emission measure distributed uniformly with temperature for $kT < kT_{\rm max}$. norm$_{\rm mek}$ is the normalization of the thermal plasma given as $\int n_{\rm e} n_{\rm H} {\rm d}V/(4\pi D^2)$ in units of 10^{-20} cm^{-5}, where $n_{\rm e}$ and $n_{\rm H}$ are the electron and hydrogen number densities, respectively, V is volume and D is the distance. Parameters and uncertainties marked with † are constrained by the limits of the fit range. P is the null hypothesis probability corresponding to χ^2/ν.

Source	$kT_{\rm max}$	norm$_{\rm mek}$ (keV)	χ^2/ν	P
49	$20.0\dagger^{+0\dagger}_{-8.4}$	$2.3^{+0.3}_{-0.2}$	28/19	9.3×10^{-2}
61	$0.45^{+0.09}_{-0.06}$	$4.9^{+0.8}_{-0.8}$	20/19	0.37
120	$7^{+13\dagger}_{-6}$	$2.2^{+0.5}_{-0.5}$	8/11	0.67
140	$4.72^{+0.30}_{-0.25}$	236^{+3}_{-4}	688/165	$< 10^{-30}$
179	$20\dagger^{+0\dagger}_{-19}$	$0.38^{+0.20}_{-0.13}$	6/4	0.24

5 DISCUSSION

5.1 Distinguishing Galactic stars from extragalactic objects

The overall X-ray spectral shapes of the Galactic stars could be reproduced by an optically thin thermal model with a distribution of temperatures. This is broadly consistent with observations of nearby stars with active coronae (e.g. Guedel et al. 2001). The characteristic shape of their X-ray spectra, and the statistical rejection of the power-law model, mean that these stars can be distinguished from the majority of the BLAGN by their EPIC X-ray spectra alone. This has considerable potential for the identification of Galactic stars in *XMM–Newton* surveys, independent of optical spectroscopy. In the 13$^{\rm H}$ field, it provides confirmation that sources 49, 61, 120 and 140, have been correctly identified as Galactic stars. For source 141, the signal to noise of the X-ray spectrum is not sufficient to confirm or reject its identification as a Galactic star.

5.2 Spectral slopes of the extragalactic sources

The distribution of best-fitting power-law slopes is shown in Fig. 5. The distribution for all sources appears to be bimodal, with the larger peak at $\Gamma \sim 1.9$ and the smaller peak at $\Gamma \sim 0.6$. However, when the distribution is broken into BLAGN, NELGs and galaxies it can be seen that the peak at $\Gamma \sim 0.6$ comes almost entirely from the NELGs, of which a similar number have $\Gamma \sim 0.6$ as have $\Gamma \sim 1.9$. The BLAGN power-law slopes show no indication of bimodality. The power-law slopes are shown as a function of redshift in Fig. 6. The slopes of the BLAGN show no trend with redshift, and are distributed relatively symmetrically around $\Gamma \sim 1.9$ at all redshifts. The distribution of NELG and galaxy spectral slopes also shows no obvious trend with redshift.

The most outlying BLAGN photon indices (at $\Gamma < 1$ and $\Gamma > 3$) come from spectra which are not well fitted with a power-law model. In contrast, the majority of the NELG spectra with $\Gamma < 1$ are acceptably fitted with a power law, perhaps because they have on average fewer counts in their X-ray spectra than the BLAGN. Each of the seven hard spectrum NELGs which have $\Gamma < 1$ in the power-law fit can also be fitted with an absorbed ($\Gamma = 1.9$) power law. Although the individual spectra do not have good enough statistics to discriminate between the two models, we can compare the goodness of fit for the two models using the total χ^2/ν for the seven objects. For the power-law model, the total $\chi^2/\nu = 75/43$, corresponding to a null hypothesis probability of 1.8×10^{-3}, whereas the total $\chi^2/\nu = 66/43$ for the absorbed power-law model, corresponding to a null hypothesis probability of 1.4×10^{-2}. Thus overall, the model with photoelectric absorption produces a better fit to the spectra of these seven hard-spectrum NELGs than the unabsorbed power-law model.

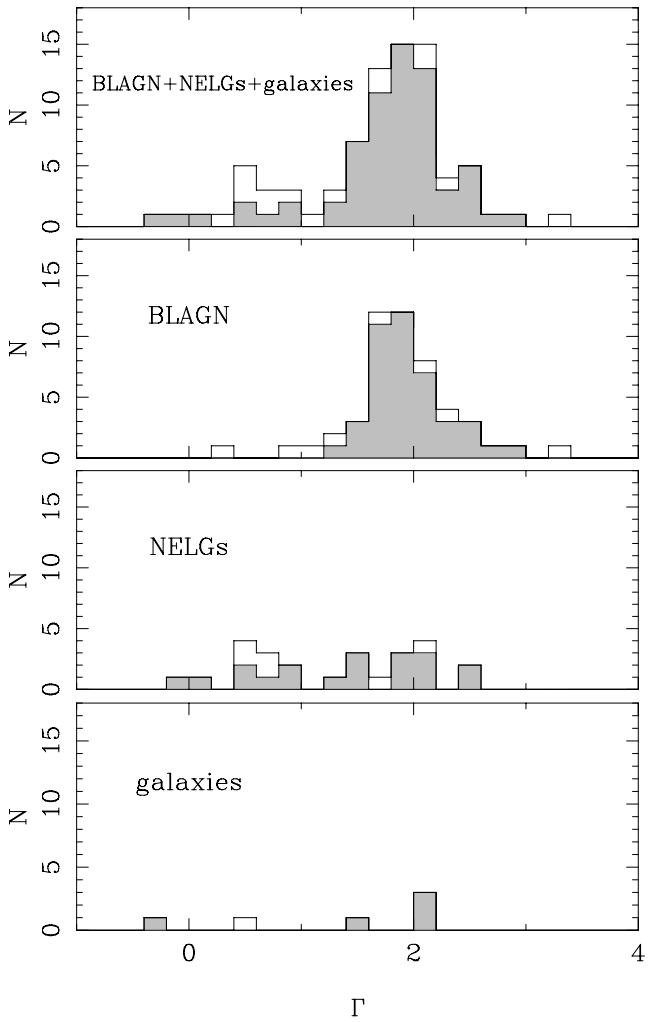

Figure 5. Best-fitting power-law indices for the different extragalactic point sources. The filled region corresponds to those sources which are acceptably fitted with a single power law.

The sample of galaxies is much smaller than the sample of NELGs, and there are only two objects with best-fitting $\Gamma < 1$, one of which is acceptably fitted with a power-law model, and one of which is not. Both of these objects are fitted well with an absorbed $\Gamma = 1.9$ power law. Overall, these results suggest that photoelectric absorption is responsible for all of the spectra which appear to have $\Gamma < 1$ in power-law model fits.

Only a small proportion (5/50) of the BLAGN show significant evidence for absorption, hence for the BLAGN we can obtain a good estimate of the intrinsic distribution of spectral slopes. For this, we assume a Gaussian distribution of spectral slopes and use the maximum likelihood method of Maccacaro et al. (1988) which takes into account the statistical errors on the individual spectral fits. We exclude the five sources which show evidence for photoelectric absorption because it is difficult to determine the intrinsic spectral shape for these sources. Three of the BLAGN appear to have

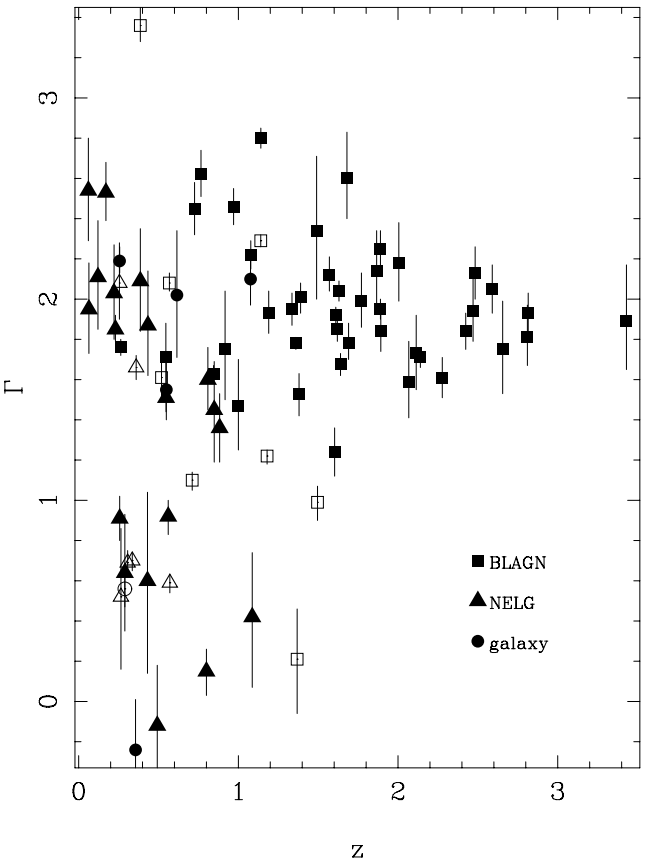

Figure 6. Best-fitting power-law slopes from single power-law model fits, shown for the different source types as a function of redshift. Poor fits are shown with open symbols.

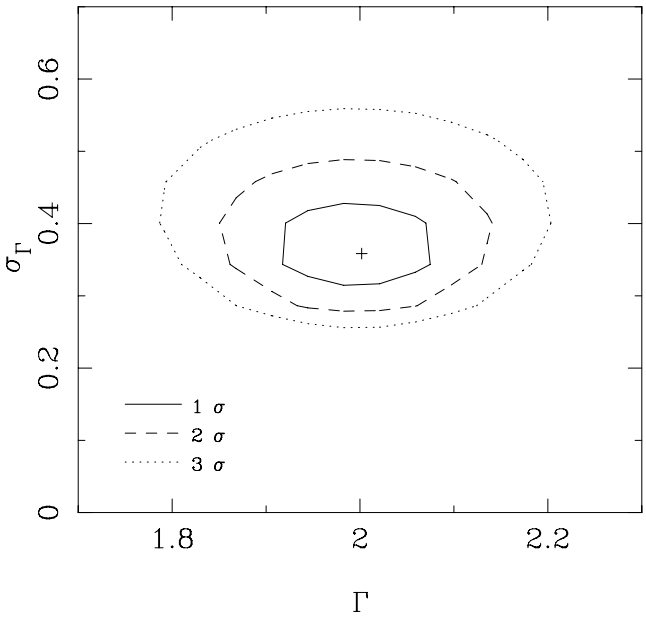

Figure 7. Maximum likelihood confidence intervals for the mean spectral index $\langle \Gamma \rangle$ and standard deviation σ_Γ of BLAGN power-law spectral indices assuming a Gaussian distribution. The three contours correspond to 1, 2 and 3σ for two interesting parameters (i.e. $\Delta S = 2.3$, 6.2 and 7.8 where $S = -2 \log_e L$ and L is the likelihood function).

spectra which are more complex than a power law, but we include these objects with their best-fitting single power-law indices when calculating the distribution. The likelihood contours for the mean of the distribution $\langle \Gamma \rangle$ and the intrinsic dispersion σ_Γ are shown in Fig. 7. The one-dimensional confidence intervals are $\langle \Gamma \rangle = 2.00 \pm 0.11, \sigma_\Gamma = 0.36^{+0.10}_{-0.07}$.

Our best-fitting $\langle \Gamma \rangle$ is entirely consistent with that found by Mateos et al. (2005b) for a comparable sample of BLAGN in the Lockman Hole, and with that found by Mateos et al. (2005a) for a larger, but brighter sample of BLAGN studied with *XMM–Newton*. Indeed, $\langle \Gamma \rangle = 2.00 \pm 0.11$ is also consistent with the value of $\langle \Gamma \rangle = 2.05 \pm 0.05$ determined by Mittaz et al. (1999) for AGN in the soft X-ray *ROSAT* International X-ray Optical Survey (RIXOS). However, the value of σ_Γ found in the $13^{\rm H}$ field is somewhat larger than that found by Mateos et al. (2005a) and Mateos et al. (2005b), who obtained $\sigma_\Gamma = 0.21^{+0.05}_{-0.04}$ and $\sigma_\Gamma = 0.20 \pm 0.04$, respectively (their confidence intervals are 90 per cent), and it is smaller than the $\sigma_\Gamma = 0.55 \pm 0.05$ obtained by Mittaz et al. (1999) for RIXOS AGN. It is likely that the large dispersion found with *ROSAT* is due to the fact that photoelectric absorption and AGN soft excess emission were both difficult to distinguish from a power law with the crude *ROSAT* Position Sensitive Proportional Counter (PSPC) spectra. Furthermore, photoelectric absorption and AGN soft excess emission both have a larger effect in the 0.1–2 keV band of the PSPC than in the 0.2–12 keV band of EPIC.

5.3 Spectra which are more complex than a power law with cold photoelectric absorption

There were five BLAGN and four NELGs which show spectra which are not well fitted with a power-law and cold absorber model. Here we discuss these objects in more detail, starting with the BLAGN.

It is likely that the poor fit of the power-law model to sources 65 and 113 owes more to the fact that they are among the best BLAGN spectra in terms of signal to noise ratio, than to a particularly large degree of curvature relative to the other BLAGN (Fig. 1). However, source 52 appears to show a more substantial departure from a single power-law spectrum, showing a very soft spectrum below 2 keV, but a much harder spectrum at higher energy. This source showed a very soft spectrum in the original *ROSAT* survey (McHardy et al. 1998), and is a luminous example of a narrow-line Seyfert 1. It was studied in its own right by Dewangan et al. (2001). The spectrum of source 52 in Fig. 1, shows significant similarity to the spectrum of the nearby narrow-line Seyfert 1 galaxy 1H 0707−495. In particular, 1H 0707−495 also has a very steep spectrum ($\Gamma = 3.8$) when fitted with a single power law over the full *XMM–Newton* energy range, but has a much flatter spectrum above 2 keV (Boller et al. 2002). The most remarkable feature of the spectrum of 1H 0707−495 is a large edge at 7–7.6 keV and a significant deficit of counts at energies higher than this (Boller et al. 2002; Gallo et al. 2004). For source 52 at $z = 0.386$, a similar edge would be redshifted to 5–5.5 keV. Source 52 is not detected beyond this energy, so it could harbour a similar edge feature to 1H 0707−495. However, the spectrum is not good enough for us to determine with confidence whether such an edge is present at this energy.

Of the five BLAGN which show absorption, three are well fitted with a power-law and cold photoelectric absorption, while sources 101 and 132 require more complicated models. Acceptable fits are found for these two sources when an additional soft emission component is included, or when the neutral absorber is replaced by

an ionized one. In the model fits including an additional soft line emitting or unabsorbed power-law component, source 132 has a soft component which emits between 5 per cent and 21 per cent as much power in the 0.2–1 keV band (observer frame) as the primary power-law component. For source 101 the additional soft component is much more important, emitting 35–120 per cent as much radiation in the 0.2–1 keV band as the primary power law. In both cases the additional soft component emits $>10^{42}$ erg s^{-1} in the 0.2–1 keV band: such a high X-ray luminosity exceeds even the most X-ray luminous starburst galaxy known (Moran, Lehnert & Helfand 1999). It is also unlikely that the soft emission comes from a group or cluster of galaxies in which the source is embedded because at such luminosities the X-ray emitting gas would be expected to have $kT \sim 1$ keV (Helsdon & Ponman 2000), whereas the best-fitting temperatures are much lower than this in the mekal fits. Furthermore, sources 101 and 132 are consistent with point sources in the X-ray images, and are isolated, separated by more than 1 arcmin from their nearest *XMM–Newton* or *Chandra* neighbours. Therefore, if these sources do have an additional soft component, it must be scattered or reprocessed AGN emission. While this is plausible for source 132, in which the soft component is ∼10 per cent as luminous as the primary AGN emission, for source 101 a scattered component would have a luminosity of more than a third of the primary component, which is untenable. The alternative, an ionized absorber, provides a good fit to both spectra, and is the only realistic hypothesis for source 101.

The situation is quite different for the four absorbed NELGs which are not well fitted with a power-law and neutral photoelectric absorption. For three of these, sources 100, 109 and 225, the ionized absorber model does not fit the data, and an additional soft component is therefore necessary. In the case of source 109, the additional soft component is likely to be due to contamination of the X-ray spectrum from the bright BLAGN, source 113, which is only 20 arcsec distant. Indeed, in the fit to source 109 with a mekal component, kT pegs at 10 keV, which is the maximum value that we allowed in the fit. At such a high temperature the mekal component is contributing more continuum than line emission, consistent with the hypothesis that the excess flux in the lowest energy channels of source 109 is actually continuum emission from source 113.

For source 225 the best-fitting mekal component has $kT = 0.8$ keV, and a 0.2–1 keV luminosity of 10^{42} erg s^{-1}, larger than that of the power-law component in the same band. This luminosity is too large for either a starburst or scattered AGN emission to be plausible. However, source 225 is one of the seven extended X-ray sources identified with 'EMLDETECT' (Loaring et al. 2005), with a FWHM extent of ∼17 arcsec, so a significant fraction of the X-ray emission is likely to originate in a group or cluster of galaxies. The temperature and luminosity of source 225 are consistent with the L_X –T_X relationship observed in galaxy groups (Helsdon & Ponman 2000), further supporting this explanation.

In source 100 the soft component has a relatively low luminosity (10^{41} erg s^{-1} in the 0.2–1 keV band), equivalent to ∼5 per cent of the primary power-law emission in the same band. Therefore, scattered emission from the AGN and hot gas from a starburst are both tenable explanations for the soft component in this source.

In the fit to source 175 including a mekal component, we obtain a very reasonable $kT = 0.2$ keV, but a soft component 0.2–1 keV luminosity of 2×10^{43} erg s^{-1}. This is equivalent to 30–50 per cent of the luminosity of the power-law component in the same band, hence neither a starburst contribution, nor scattered AGN emission are feasible explanations. It is possible that a nearby X-ray source contributes to the soft emission: *Chandra* source number 159 from McHardy et al. (2003) is only 11 arcsec distant, but is a factor of 10 fainter than source 175, and a visual inspection of the *XMM–Newton* 0.2–0.5 keV image indicates that this source does not contribute significantly. Therefore, it appears that an ionized absorber is a better hypothesis for the X-ray spectral shape of source 175 than an additional soft component.

5.4 The luminosity distribution as a function of optical class

In Fig. 8, we show the 2–10 keV luminosities (L_{2-10}) as a function of redshift for the extragalactic sources. The luminosities are for the primary power-law component only, are corrected for intrinsic and Galactic absorption, and are derived from the most realistic model fit to each source, as discussed in the text. At $z > 1$, optical spectroscopic identification of NELGs and galaxies is extremely difficult compared to BLAGN, so it is not surprising that the vast majority of optically identified sources at $z > 1$ are BLAGN. Therefore, it is useful to restrict our attention to $z < 1$, where we are able to identify the full range of optical counterparts, in order to examine the luminosity and absorption characteristics of the NELGs and galaxies with respect to the BLAGN. For $z < 1$, we see in Fig. 8 that the majority (13/15) of the X-ray absorbed sources are NELGs or galaxies, as expected in AGN unification schemes. However, the majority (15/29) of the NELGs and galaxies in this redshift range (i.e. $z < 1$) *do not* show significant X-ray absorption. The NELGs and galaxies span the full $z < 1$ X-ray luminosity range, but the X-ray absorbed sources are only found at $L_{2-10} > 10^{42}$ erg s^{-1}.

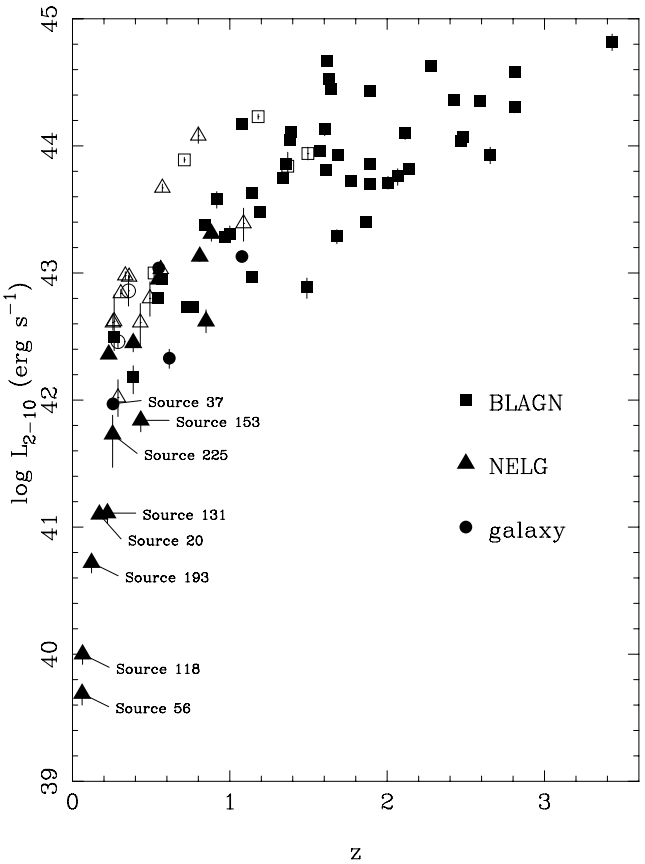

Figure 8. 2–10 keV intrinsic rest-frame luminosities as a function of redshift. The sources which show X-ray absorption in their X-ray spectra are shown with open symbols, while sources without significant X-ray absorption are shown with closed symbols.

Indeed, the X-ray absorbed sources have a higher mean 2–10 keV luminosity ($\langle L_{2-10}\rangle = 2 \times 10^{43}$ erg s^{-1}) than the unabsorbed sources, which have $\langle L_{2-10}\rangle = 8 \times 10^{42}$ erg s^{-1}. However the mean luminosity of the NELGs and galaxies ($\langle L_{2-10}\rangle = 10^{43}$ erg s^{-1}) is smaller than the mean luminosity of the BLAGN ($\langle L_{2-10}\rangle = 2 \times 10^{43}$ erg s^{-1}).

5.5 The origin of the X-ray emission in the low-luminosity extragalactic sources

For sources with $L_{2-10} > 10^{42}$ erg s^{-1}, the presence of an AGN is unambiguous. However, the lower-luminosity X-ray sources could plausibly be powered by star formation, in which case the X-rays will be a composite of emission from massive X-ray binaries and optically thin thermal emission from hot interstellar gas within the galaxy. Therefore, to determine whether the X-ray emission from these objects is powered by AGN, we must examine them in more detail on a case-by-case basis.

The two lowest luminosity sources, 56 and 118, have L_{2-10} of 5×10^{39} and 1×10^{40} erg s^{-1}, respectively. They are both detected as point sources with *XMM–Newton* but are not detected with our point source searching method in the *Chandra* images (McHardy et al. 2003; Loaring et al. 2005), suggesting that the X-ray emission is significantly extended with respect to the *Chandra* PSF (i.e. on a scale comparable to the optical galaxy). They are both bright radio sources (>0.5 mJy at 1.4 GHz), extended on a similar scale to the optical galaxy (Seymour et al. 2004) and so almost certainly powered by star formation. The starburst nature of source 56 is discussed at length in Gunn et al. (2001). In Fig. 2 we see that although the spectra are consistent with a power-law shape, both have a low-significance peak at ∼0.7 keV, consistent with thermal emission from a starburst. Thus, the X-ray emission from both source 56 and source 118 could quite plausibly be powered by star formation.

In contrast, the sources with $L_{2-10} > 2 \times 10^{40}$ erg s^{-1} are much more likely to be AGN powered. Sources 20, 131 and 193 (all NELGs) show no evidence for thermal gas components in their spectra, which are consistent with power laws, suggesting that they are AGN. Both sources 131 and 193 are detected as point sources in the *Chandra* images (McHardy et al. 2003), consistent with this hypothesis. Source 20 was not detected with *Chandra*, but in this case variability, rather than spatial extent, is responsible. Source 20 was more than a factor of 2 brighter during *XMM–Newton* revolution 0276 than it was 11 d later in revolution 282, and hence the emission must come from an AGN rather than a multitude of sources within the galaxy.

At higher luminosities, the hypothesis that star formation powers the X-ray emission becomes even less likely. Source 225 has a thermal component in its X-ray spectrum, but as discussed in Section 5.3 the X-ray emission is extended on a scale larger than the optical galaxy in this source, so the thermal emission is due to a group or cluster of galaxies. Source 153 is not detected at 1.4 GHz (Seymour et al. 2004), so is unlikely to be a vigourously star forming galaxy, while source 37 is almost certainly a BL Lac object (Gunn et al. 2003; Moss et al., in preparation).

From the case-by-case examination of the eight sources with $L_{2-10} < 10^{42}$ erg s^{-1}, only the two lowest luminosity objects, 56 and 118, which have $L_{2-10} \leqslant 10^{40}$ erg s^{-1}, appear to have X-ray emission dominated by star formation. In all the other cases the 2–10 keV X-ray emission appears to be AGN dominated. Apart from source 225, the AGN is also dominant in the 0.5–2 keV band in these objects.

5.6 The nature of the NELGs and galaxies without X-ray absorption

Excepting objects which are powered by star formation, the standard paradigm for X-ray selected NELGs and absorption-line galaxies is that they are obscured AGN (e.g. Hasinger et al. 2001; Barcons et al. 2002; Mainieri et al. 2002). However in the 13$^{\rm H}$ field, a significant number of the X-ray sources which are optically classified as NELGs and galaxies contain AGN (see Section 5.5) which do *not* show evidence for X-ray absorption. While for three of these objects (sources 94, 153 and 117), the current data do not allow us to rule out an absorber with a significant column density ($N_{\rm H} > 10^{22}$ cm^{-2}), for more than half (8/14) of these objects the data imply $N_{\rm H} \leqslant 3 \times 10^{21}$ cm^{-2} (Table 8, excluding objects 56 and 118 which are likely powered by star formation). For a Galactic gas to dust ratio and reddening curve (Bohlin, Savage & Drake 1978), this would correspond to at most a factor of 3 attenuation to the broad Hα line. For some of the lower-redshift objects the $N_{\rm H}$ limits are so restrictive that optical reddening of the AGN should be negligible, e.g. source 20 has $N_{\rm H} < 2.6 \times 10^{20}$ cm^{-2}. Silverman et al. (2005) reported a number of objects in the *Chandra* Multiwavelength Project which appear to have similar properties and argued that this can be attributed to dilution of the AGN emission by the host galaxy light (see also Page et al. 2003; Severgnini et al. 2003).

The dilution hypothesis can be investigated by comparing the optical to X-ray flux ratios as a function of optical classification. The X-ray flux is completely dominated by the AGN component, while the optical flux comes largely from the AGNs in sources classified as BLAGNs but is dominated by the host galaxy in sources classified as NELGs and galaxies (Loaring et al. in preparation). Fig. 9 shows the 2–10 keV flux of unabsorbed galaxies and NELGs with $z < 0.8$, against the *R*-band optical magnitude from McHardy et al. (2003). Sources 56 and 118 are not shown, because their X-ray emission is likely to be powered by stellar processes. Fig. 9 is restricted to sources with $z < 0.8$ so that the *R* band corresponds to rest-frame optical emission longward of the Balmer break. The solid line in Fig. 9 corresponds to the mean optical/X-ray ratio of the six BLAGN that are shown. The dashed lines correspond to ±0.5 dex about this ratio, which is approximately the standard deviation of

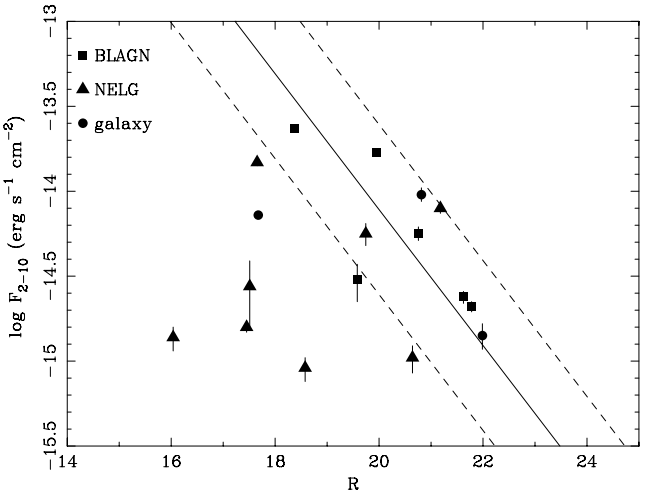

Figure 9. 2–10 keV flux against *R* magnitude, for unabsorbed X-ray sources with $z < 0.8$. The solid line corresponds to the unweighted mean X-ray/optical ratio of the BLAGN shown, and the dashed lines delimit ±0.5 dex around this ratio.

optical/X-ray ratios found for X-ray selected BLAGN (Ciliegi et al. 1995). The NELGs are distributed over a broader region of Fig. 9 than the BLAGN, and more than half of the NELGs lie to the left-hand side of the region enclosed by the dashed lines, i.e. they have a larger optical/X-ray flux ratio than most of the BLAGN. Four of the NELGs are more than 3 mag to the left-hand side of the solid line in Fig. 9. Therefore, if they host active nuclei with optical/X-ray flux ratios typical for the BLAGN in Fig. 9, the nuclear component will be outshone by more than a factor of 15 in the optical by the surrounding galaxy. Two of the NELGs and one galaxy lie 1.5–2.5 mag to the left-hand side of the solid line, suggesting that the active nucleus will be outshone by the host galaxy by factors of 3–10; dilution of the AGN component by starlight could reasonably explain the absence of broad emission lines in the optical spectra of these objects. The four remaining NELGs and galaxies, which lie within the region bounded by the dashed lines, have optical/X-ray ratios similar to those of the BLAGN. In these objects, the stellar component produces a similar flux of optical radiation as we would expect to observe from the nucleus, given the X-ray flux. For dilution of the nuclear spectrum by galaxy starlight to explain the optical characteristics of these sources, their nuclear components must have optical/X-ray flux ratios which are smaller than the average for BLAGN. This however, is quite plausible if AGN with $L_{2-10} < 10^{43}$ erg s^{-1} have a similar intrinsic scatter of optical/X-ray flux ratios to the scatter found in more luminous BLAGN ($\sim$0.5 dex; Ciliegi et al. 1995). The lack of NELGs and galaxies to the right-hand side of the dashed-line region of Fig. 9 is consistent with this picture: starlight is unlikely to render the broad emission lines unidentifiable when the host galaxy has a low luminosity compared to the nucleus, unless the optical/X-ray flux ratio of the nucleus is unusually low.

Fig. 9 therefore implies that in the NELGs and galaxies which do not show significant X-ray absorption, the lack of broad optical emission lines could be due to the low contrast of the emission lines against the much stronger starlight component. However, it should be noted that there are alternative hypotheses that are not presently ruled out. These objects could possess absorbing media with a high dust to gas ratio, and/or in which the gas is ionized and so its X-ray photoelectric opacity is reduced (Pappa et al. 2001). Discrimination between these hypotheses will require high spatial resolution, high signal to noise optical spectra (Severgnini et al. 2003). Alternatively, some of these objects could be BL Lac objects; this appears to be the case for at least source 37 (Gunn et al. 2003; Moss et al. in preparation).

We calculated the absolute magnitudes M_R for the 11 NELGs and galaxies shown in Fig. 9. The results are given in Table 11, and were calculated using the elliptical galaxy K-corrections from Coleman, Wu & Weedman (1980). These objects lie in the bright part of the galaxy luminosity function, having absolute magnitudes of around M_R^* or brighter, where M_R^* ($\sim$21.8 for $H_0 = 70\,\mathrm{km\,s^{-1}\,Mpc^{-1}}$; Trentham, Sampson & Banerji 2005) defines the knee in the luminosity function. On the other hand, they are all host AGN which have $L_{2-10} < 2 \times 10^{43}$ erg s^{-1}), lower than the knee in the X-ray luminosity function (e.g. Page et al. 1997; Barger et al. 2005; Hasinger, Miyaji & Schmidt 2005). This combination of weak AGN and luminous host galaxies, given the $M_\bullet$–σ relation (Ferrarese & Merritt 2001), suggests that these objects host massive black holes ($\geqslant 10^8\,\mathrm{M}_\odot$, Page 2001) with low Eddington ratios (<1 per cent). Such objects are not low-mass objects formed at late times, the result of AGN 'cosmic downsizing' as argued by Barger et al. (2005), but are instead the relatively inactive remnants of once-luminous AGN.

Table 11. Absolute magnitudes M_R for the $z < 0.8$ galaxies and NELGs that contain an AGN, and which do not show significant X-ray absorption.

Source	M_R
1	−22.306
20	−22.303
37	−23.175
103	−22.169
115	−22.892
117	−21.896
131	−21.872
153	−21.814
184	−22.550
193	−22.834
225	−23.317

6 CONCLUSIONS

We have presented the *XMM–Newton* EPIC X-ray spectra of 86 X-ray sources in the 13^H field which have optical identifications and > 70 X-ray counts. More than half of the sources are BLAGN, and the majority of these (42/50) have spectra which are consistent with a power-law shape. The photon indices are distributed about a mean $\langle\Gamma\rangle = 2.0 \pm 0.1$ with an intrinsic dispersion of $\sigma_\Gamma = 0.4 \pm 0.1$. Of the eight BLAGN which have X-ray spectra inconsistent with a power-law shape, three have curvature with excess emission at the high- and low-energy ends relative to a power law, and five show evidence for absorption at soft X-ray energies. The addition of a cold photoelectric absorber yields an acceptable fit for three of these objects, one requires an ionized absorber, and the remaining object can be fitted with either an ionized absorber or with an additional component of scattered or reprocessed soft X-ray emission.

Of the 25 NELGs, 13 have absorbed X-ray spectra, nine of which can be fitted with a cold photoelectric absorber and four of which require a more complex model with either an ionized absorber or an additional component of soft X-ray emission. Of the six absorption-line galaxies in the sample, two show evidence for X-ray absorption, and both are consistent with a simple cold photoelectric absorber. Of the 12 NELGs which do not show evidence for X-ray absorption, two have X-ray properties which suggest that their X-ray emission is powered by star formation. The other 14 NELGs and galaxies which are not X-ray absorbed have X-ray properties implying the presence of an AGN. At least at $z < 0.8$, where our R-band imaging probes the rest-frame optical starlight, these objects are luminous galaxies ($M_R > M_R^*$), containing relatively low X-ray luminosity AGN ($L_{2-10} < 2 \times 10^{43}$ erg s^{-1}), and the lack of AGN signatures in the optical could be due to the dilution of the AGN radiation by the bright host galaxy. These objects are likely to be massive black holes ($>10^8\,\mathrm{M}_\odot$) accreting with low Eddington ratios (<0.01), rather than vigorous, low-mass black holes.

Finally, the sample contains five Galactic stars which have X-ray spectra consistent with optically thin thermal emission with a broad distribution of temperature, consistent with active stellar coronal emission. In four of the five stars, the X-ray spectra alone can distinguish them from AGN at similar X-ray flux levels.

ACKNOWLEDGMENTS

Based on observations obtained with *XMM–Newton*, an ESA science mission with instruments and contributions directly funded by ESA Member States and NASA. The William Herschel Telescope

is operated on the island of La Palma by the Isaac Newton Group in the Spanish Observatorio del Roque de los Muchachos of the Instituto de Astrofisica de Canarias. The W. M. Keck Observatory is operated as a scientific partnership among the California Institute of Technology, the University of California and the National Aeronautics and Space Administration and was made possible by the generous financial support of the W. M. Keck Foundation. We thank Sergey Kuznetsov for helpful comments.

REFERENCES

Alexander D. M. et al., 2003, AJ, 126, 539
Anders E., Grevesse N., 1989, Geochim. Cosmochim. Acta, 53, 197
Antonucci R., 1993, ARA&A, 31, 473
Barcons X. et al., 2002, A&A, 382, 522
Barcons X., Carrera F. J., Ceballos M. T., 2003, MNRAS, 339, 757
Barger A. J. et al., 2003, AJ, 126, 632
Barger A. J., Cowie L. L., Mushotzky R. F., Yang Y., Wang W.-H., Steffen A. T., Capak P., 2005, AJ, 129, 578
Bohlin R. C., Savage B. D., Drake J. F., 1978, ApJ, 224, 132
Boller Th. et al., 2002, MNRAS, 329, L1
Caccianiga A. et al., 2004, A&A, 416, 901
Ciliegi P., Elvis M., Wilkes B. J., Boyle B. J., McMahon R. G., Maccacaro T., 1995, MNRAS, 277, 1463
Coleman G. D., Wu C.-C., Weedman D. W., 1980, ApJS, 43, 393
Comastri A., Setti G., Zamorani G., Hasinger G., 1995, A&A, 296, 1
Crawford C. S., Gandhi P., Fabian A. C., Wilman R. J., Johnstone R. M., Barger A. J., Cowie L. L., 2002, MNRAS, 333, 809
Dewangan G. C., Singh K. P., Jones L. R., McHardy I. M., Mason K. O., Newsam A. M., 2001, MNRAS, 325, 1616
Dwelly T., Page M. J., Loaring N. S., Mason K. O., McHardy I., Gunn K., Sasseen T., 2005, MNRAS, 360, 1426
Franceschini et al., 2003, MNRAS, 343, 1181
Gallo L. C., Tanaka Y., Boller Th., Fabian A. C., Vaughan S., Brandt W. N., 2004, MNRAS, 353, 1064
Giacconi R. et al., 2002, ApJS, 139, 369
Gilli R., Risaliti G., Salvati M., 1999, A&A, 347, 424
Guedel M. et al., 2001, A&A, 365, L336
Gunn K. F. et al., 2001, MNRAS, 324, 305
Gunn K. F. et al., 2003, AN, 324, 105
Hasinger G., Burg R., Giacconi R., Schmidt M., Trumper J., Zamorani G., 1998, A&A, 329, 482
Hasinger G. et al., 2001, A&A, 365, L45
Hasinger G., Miyaji T., Schmidt M., 2005, A&A, 441, 417
Helsdon S. F., Ponman T. J., 2000, MNRAS, 315, 356
Kinkhabwala A. et al., 2002, ApJ, 575, 732
Loaring N. S. et al., 2005, MNRAS, 362, 1371
Maccacaro T., Gioia I. M., Wolter A., Zamorani G., Stocke J. T., 1988, ApJ, 326, 680
Mainieri V., Bergeron J., Hasinger G., Lehmann I., Rosati P., Schmidt M., Szokoly G., Della Ceca R., 2002, A&A, 393, 425
Mainieri V. et al., 2005, A&A, 437, 805
Maiolino R., Marconi A., Salvati M., Risaliti G., Severgnini P., Oliva E., La Franca F., Vanzi L., 2001, A&A, 365, 28
Mateos S. et al., 2005a, A&A, 433, 855
Mateos S., Barcons X., Carrera F. J., Ceballos M. T., Hasinger G., Lehmann I., Fabian A. C., Streblyanska A., 2005b, A&A, 444, 79
McHardy I. M. et al., 1998, MNRAS, 295, 641
McHardy I. M. et al., 2003, MNRAS, 342, 802
Merritt D., Ferrarese L., 2001, ApJ, 547, 140
Mittaz J. P. D. et al., 1999, MNRAS, 308, 233
Moran E. C., Lehnert M. D., Helfand D. J., 1999, ApJ, 526, 649
Page M. J., 2001, MNRAS, 328, 925
Page M. J., Mason K. O., McHardy I. M., Jones L. R., Carrera F. J., 1997, MNRAS, 291, 324
Page M. J., Mittaz J. P. D., Carrera F. J., 2001, MNRAS, 325, 575
Page M. J. et al., 2003, AN, 324, 101
Page M. J., Davis S. W., Salvi N. J., 2003, MNRAS, 343, 1241
Pappa A., Georgantopoulos I., Stewart G. C., Zezas A. L., 2001, MNRAS, 326, 995
Sako M., Kahn S. M., Paerels F., Liedahl D. A., 2000, ApJ, 543, L115
Setti G., Woltjer L., 1989, A&A, 224, L21
Severgnini P. et al., 2003, A&A, 406, 483
Seymour N., McHardy I. M., Gunn K. F., 2004, MNRAS, 352, 131
Silverman J. D. et al., 2005, ApJ, 618, 123
Strüder L. et al., 2001, A&A, 365, L18
Treister E. et al., 2004, ApJ, 616, 123
Trentham N., Sampson L., Banerji M., 2005, MNRAS, 357, 783
Turner T. J., George I. M., Nandra K., Mushotzky R. F., 1997, ApJS, 113, 23
Turner M. J. L. et al., 2001, A&A, 365, L27

This paper has been typeset from a TEX/LATEX file prepared by the author.